# Sustainable Conversion of Lignocellulose to High-Purity, Highly Crystalline Flake Potato Graphite

Nathan A. Banek, Dustin T. Abele, Kevin R. McKenzie, Jr., and Michael J. Wagner*

Department of Chemistry, George Washington University, Washington, D.C. 20052, United States

**S** *Supporting Information*

**ABSTRACT:** The carbon net negative conversion of biochar, the byproduct of pyrolysis bio-oil production from biomass, to very high-purity (99.95%), highly crystalline flake graphite that is essentially indistinguishable from high-grade commercial Li-ion grade graphite, is reported. The flake size of the graphite is determined by the physical dimensions of the metal particles imbedded in the biochar, demonstrated in the range of micrometers to millimeters. "Potato"-shaped agglomerates of graphite flakes result when the flake diameter is in the 1−5 μm range. The process is shown to work with a variety of biomass, including raw lignocellulose (sawdust, wood flour, and corn cob) and biomass components (cellulose and lignin), as well as lignite. The synthesis is extremely rapid and energy efficient (0.25 kg/kWh); the graphite is produced with a very high yield (95.7%), and the energy content of its coproduct, bio-oil, exceeds that needed to power the process. The demonstrated process is a tremendous advance in the sustainability of graphite production, currently commercially mined or synthesized with very high environmental impacts, and results in a value-added product that could economically advantage carbon-neutral bio-oil production.

**KEYWORDS:** *Bio-oil, Biochar, Pyrolysis Oil, Biomass, Li-ion battery*
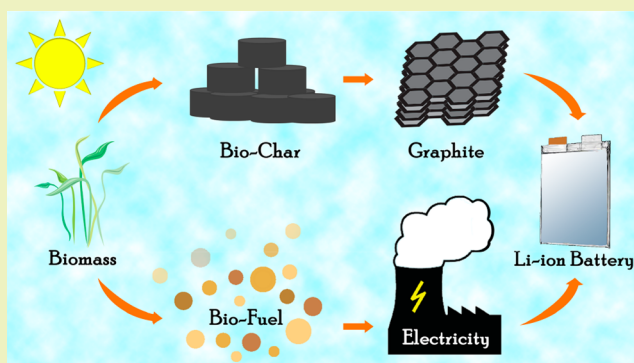


## INTRODUCTION

Most scenarios that meet the Paris Agreement goal of limiting global warming to 2 °C rely on the widespread adoption of sustainable bioenergy and on carbon valuation for economic viability.[1] Carbon pricing (e.g., carbon tax or emission permits) would not be necessary if market competitive solutions are found; however, this is extremely challenging. One potentially competitive solution, lignocellulose pyrolysis, is a nascent technology that has attracted considerable recent interest as a method of sustainable and carbon-neutral electricity and liquid biofuel production.[2] In addition to a number of smaller projects around the world, a full-scale combined heat and power plant (district heat, 210 GWh electricity, and 50,000 ton/year bio-oil) is currently operational in Joensuu, Finland. Pyrolysis oil is particularly attractive because it is the least expensive carbon-neutral liquid biofuel appropriate for transportation, a market sector that accounts for 27% of all greenhouse emissions, but it is currently more expensive than fossil fuels.[3] While advances in bio-oil upgrading could improve its economic outlook[4−8] so too could processes that produce value-added products from biochar, the carbonaceous waste product of pyrolysis that is currently returns little as a relatively low energy solid fuel or material for soil amendment.[2,9,10]

The very high carbon content of biochar suggests graphite as a potential valorization product. Graphite is classified as a "strategic and critical mineral" by the U.S. and E.U., with a market that is expected to reach 4.48 million tons and $17.56 billion by 2020.[11] It has a wide range of applications, including uses in electrodes for the steel and aluminum industries, refractories, carbon risers, electric motor brushes, electrical discharge machining, brake lining, lubricants, neutron moderators, and batteries. Upgrading biochar to lithium-ion (Li-ion) battery grade graphite, increasing its value by approximately 3 orders of magnitude to $14870−18000 per ton,[12] is particularly attractive as it could also meet the material needs of the rapidly expanding market for zero-emission electric vehicles.

Graphite is an allotrope of carbon, its ideal structure composed of graphene layers stacked in a 3D crystalline lattice, with the carbon atoms of each layer nested into the center of the sp$^2$ bonded carbon hexagons of adjacent layers. Graphite commonly displays some degree of turbostratic disorder; that is, graphene sheets that are stacked, but adjacent layers are rotated, translated, or otherwise defective, resulting in imperfections in the registry of the layering, with consequently larger interlayer spacing and lack of *c*-axis crystalline order. While turbostratic carbon can have a lithium gravimetric (per

mass) storage capacity that is higher than that of graphite due to its increased porosity, commercial Li-ion batteries exclusively use graphite with extremely low turbostratic disorder as the anode active material due to its superior discharge potentials, better electrical conductivity, higher volumetric capacity, and lower irreversible losses.

Graphite is either synthesized or obtained from natural deposits. Some carbon materials, such as coke and mesophase pitch, can be transformed to graphite by heating and are thus termed graphitizable. Others are non-graphitizable, including chars formed from organic materials (e.g., lignocellulose) and certain fossil fuels (e.g., lignite) not transforming into graphite even when heated to 3000 °C at atmospheric pressure, instead forming hard carbons due to the formation of cross-linking between the layers that prevent the removal of turbostratic disorder.[13] Synthetic graphite for Li-ion batteries is made by blending high-purity graphitizable carbons (pet coke and coal tar pitch), extrusion, repeated carbonization (baking at 800−1000 °C), pitch impregnation, and finally graphitization at ∼3000 °C for several weeks. Production of synthetic graphite is environmentally detrimental because it is highly energy intensive and additionally results in large-scale (30−40% mass loss of reactants as gaseous species) non-combustion greenhouse emissions.[14]

Mining and purifying natural graphite results in devastating environmental impacts to the soil, water, and air.[15] Unlike coal, natural graphite is rarely found in veins, instead requiring large-scale benefaction by repeated crushing, milling, and floatation to separate the graphite flakes from the rock they coat ("marks"). Acid leaching, including large-scale use of HF, is performed to remove embedded minerals. High-grade (85−98%) natural flake graphite can be further upgraded to Li-ion battery grade graphite (99.9+%) by intensive purification with a large (∼70%) material loss.

Demand for high-quality flake graphite is expected to experience an extraordinary growth rate, in large part due to the 12 Li-ion battery "mega-factories" that are scheduled to begin production by 2020. These factories will triple the current production capacity to serve the rapidly growing market for electric vehicles (EV). The Tesla facility alone is expected to require the output of 4−6 new flake natural graphite mines or an equivalent quantity of synthetic graphite.[16,17] Supply constraints of both natural and synthetic graphite have led to predictions that suppliers will not be able to keep up with the demand from the rapid increase in Li-ion battery production for EVs.[16,18] Unfortunately, there are no other significant sources of Li-ion battery grade graphite.

Herein we report a novel and environmentally friendly route to transform non-graphitizable biochar to highly crystalline, high-purity (99.95%) micrometer- to millimeter-scale flake graphite that is essentially indistinguishable from high-grade (Li-ion) commercial graphite. Furthermore, the "biochar graphite" (BCG) can be formed in agglomerates that are very similar to "potato" (also termed "shaped" or "spherical") graphite, which is preferred for Li-ion battery anodes due to its low surface area after carbon coating, decreasing Coulombic losses, and a high packing efficiency, increasing volumetric and areal capacity. BCG may also be inexpensive (see the Economic Analysis in the Supporting Information) due to the low cost of biomass and Fe metal, rapid synthesis, very high yield (95.7% yield, 0.25 kg/kWh), and because the energy content of its coproduct, bio-oil,[2] exceeds the energy content needed to power the process. Thus, BCG with bio-oil

production promises to be a $CO_2$ net-negative energy producing process that could provide an environmentally benign supply of high-grade graphite to meet the rapidly growing needs of electric vehicles: electricity and graphite for Li-ion battery production.

## ■ EXPERIMENTAL SECTION

**Materials.** All materials were used as received unless otherwise noted. Unless stated otherwise in this manuscript, hardwood sawdust (CrossRoad Sales LLC) and −100 mesh (99%, Strem product no. 93-2663, flake-shaped, passed through 325 mesh sieve before use) Fe metal (−325 mesh Fe), referred to as −325 mesh Fe, were used as the starting materials. Other biomass used includes wood flour (System Three Resin, Inc.), corncobs (local grocer, dried and then ground before use), cellulose (Avicel MCC PH105), and lignin (TCI America). Lignite coal was obtained from Giverny, Inc. Other Fe metal particles used were 0.60 mm steel spheres (SuperMagnetMan.com, product no. SS006) and 1−2 mm granules (99.98%, Alfa Aesar product no. 39708). Alternatively, Ni (99.5%, −100 mesh, Strem Chemicals) or Co (99.8%, −100 mesh, Strem Chemicals) metal particles were also used.

**Synthesis of Graphite.** Typically, biomass (6.0 g) and Fe metal (2.0 g) were loaded into a hardened steel cup (80 mL, Fritsch GmbH) with six balls (hardened steel, 1 cm diameter, 10:1 ball to powder mass ratio) and milled at 300 rpm for 30 min using a planetary mill (Pulverisette 6, Fritsch GmbH). The resulting powder was pressed (10.89 t, Carver 3851 benchtop laboratory press) to form 20 mm diameter pellets. A 21/64" hole was then drilled in the center of each pellet with a drill press, and the pellets were heated under $N_2$ gas (30 mL/min) from room temperature to 600 °C at a 30 °C/min ramp rate and held for a total heating time of 30 min. While the heating temperature has a significant effect on the product distribution (bio-oil/syngas/char), varying the temperature in the range of 400−600 °C appeared to have little or no effect on the synthesis described here, other than the obvious dependence of yield on the proportion of char produced and mass loss of the char during laser exposure due to the higher proportion of volatile material in char produced at lower temperatures. The heating under inert atmosphere resulted in the evolution of bio-oil and gas and transformed the biomass to biochar. After charring at 600 °C, 40% of the original pellet mass remained (80% of sawdust mass lost) as black pellets containing biochar (37.5 wt %) and Fe (62.5 wt %). After they were cooled, the biochar/Fe pellets were skewered on a 1/4" diameter stainless steel rod which was then placed vertically into a stainless steel 4-way cross, fed through the top flange equipped with an Ultra-Torr vacuum fitting (Swagelok), and secured to a stepper motor (STM-23, Applied Motion Products). The chamber was evacuated to $10^{-3}$ Torr and then maintained at 0.5 Torr with flowing inert gas. Each pellet was then irradiated through an antireflective coated ZnSe window (Design Research Optics) by a 2 mm diameter 10.4 $\mu$m laser beam (Firestar t60, Synrad Inc., 95% power) while the pellet was rotated at a linear velocity of 1.63 mm/s (1.2 rev/min) for one full rotation, resulting in a 2.78% pellet mass loss. Finally, the material exposed to the laser was removed by cutting, and the resulting powder was lightly ground by hand in an agate mortar with a pestle.

The raw product was treated in refluxing 50% v/v HCl for 1 h, filtered, and washed with deionized $H_2O$, followed either by microwave digestion or by further refluxing HCl. Microwave digestion was performed by heating the product in $HNO_3$:HCl:$H_2O$ (1:1:2 v/v) solution (ACS grade, 68−70% $HNO_3$ and 36.5−38% HCl, VWR Scientific) using an XP-1500+ Teflon vessel and a MARS 5 digestion microwave system (CEM Corp.) from room temperature to 210 °C in 10 min and then holding it at that temperature for an additional 40 min. Note that while microwave digestion is convenient at the laboratory scale, recovery, grinding, and treatment for an additional hour in refluxing 50% v/v HCl was equally effective and may be advantageous at a larger scale as the use of microwave digestion and $HNO_3$ are avoided. After the product purified by either method was cooled to room temperature, the mixture was diluted with deionized

water and the solid product was collected by vacuum filtration (1 $\mu$m polyster, GVS LifeSciences). The product was then washed with additional deionized water until a neutral pH was obtained, rinsed with 1 M NaOH (>97% Fisher Scientific) followed by deionized water neutralization, rinsed with a 10% v/v HCl solution followed by deionized water neutralization, and finally dried under vacuum.

Silicon is commonly found in lower purity iron and some inexpensive biomass waste products, presenting itself as silica in the final product that is not removed by the purification methods described above. The removal of silica from natural graphite is extremely difficult as it is deeply embedded in the graphite, requiring multiple instances of grinding, floatation, and treatment with caustic agents (including HF), with consequential loss (up to 70 wt %) of graphite as waste and significant environmental impact. In contrast, when silicon presents itself in the BCG it is as a surface contaminant and can be removed by digestion in 2 M NaOH solution for 40 min at 210 °C.

**IR Thermometry.** The surface temperature of char/metal pellets was measured with an infrared sensor (Micro-Epsilon, CTLM1H1-CF3-C3) with a spot size of 0.7 mm diameter. The sensor was calibrated by adjusting the emissivity (0.9) setting so that the temperature reading matched that determined by a thermocouple in contact with the sample in a tube furnace at 900 °C.

**Ashing.** Porcelain crucibles and lids (23 mL, Fisher) were heated in air at 900 °C for 5 h, rinsed with deionized water, dried at 120 °C for 1 h, and then stored in a desiccator to cool them to room temperature prior to performing any experiments. All weight measurements were performed on an Ohaus Analytical Plus 250D (rated precision of 0.02 mg and linearity of 0.03 mg). Measurement precision was determined to be 0.03 mg by calculating the standard deviation of the mass of a 20 mg standard measured 10 times in a room-temperature, dry, tared crucible, allowing for the balance to return to 0.00000 g following each measurement. Mass reproducibility was determined to be within the measured precision by recording the mass of the empty crucibles before and after heating at a ramp rate of 10°/min to 900 °C, holding at that temperature for 5 h, removing the crucibles from the furnace, and cooling them to room temperature in a desiccator.

For each ash determination, graphite (300 mg) was loaded into a room-temperature, dry, preweighed crucible and its mass was determined. The crucible was then equipped with a lid and placed in a muffle furnace (Barnstead Thermolyne 1500), heated at a ramp rate of 10 °C/min to 900 °C, held at that temperature for 5 h, removed, and cooled to room temperature in a desiccator prior to measuring its final mass. Sample ash content was determined as the difference between the mass of the crucible prior to and after the heating procedure.

**Elemental Analysis.** C, H, and N (PerkinElmer 2400 Series II CHNS/O Analyzer) and O (Thermo Finnigan FlashEA Elemental Analyzer) analysis of biochar was performed by Galbraith Laboratories, Inc. Full scan trace impurity elemental analysis of graphite was performed using glow discharge mass spectrometry (GDMS) by EAG Laboratories.

**Powder X-ray Diffraction (XRD).** XRD patterns were obtained with a Rigaku Miniflex+ diffractometer using Cu K$\alpha$ radiation.

**Surface Area and Porosity Determination.** Surface area (BET method) and porosity were determined from nitrogen adsorption isotherms obtained with a Tri-Star 3000 (Micrometrics) instrument. One of the three sample measurement ports of the Tri-Star was equipped with an empty sample tube with which the saturation vapor pressure ($P_0$) of $N_2$ was measured concurrently with each measurement of the equilibrium vapor pressure ($P$) over the sample. Isotherm adsorption data were recorded from 0.05 to 0.989 $P_0/P$.

**Raman.** Raman spectra were acquired with a Horiba LabRAM HR Evolution Raman microscope equipped with a 532 nm wavelength diode laser.

**Electron Microscopy.** Scanning electron microscopy (SEM) micrographs were obtained using an FEI Teneo LV with its in-lens secondary electron detector and elemental analysis performed with its EDS detector (EDAX) using a 20 kV accelerating voltage.

**Electrode Preparation and Cycling.** Graphite anodes were formulated by combining 90 mg of BCG, 5 mg of carbon black (Super C45, Imerys TIMCAL America Inc.), 100 uL of a 10% ethanol solution (200 proof, Pharmco-Aaper), and 100 $\mu$L of 5% Li-polyacrylate binder solution prepared by dissolving poly(acrylic acid) (1000 kDa, Polysciences) in deionized water and neutralizing with LiOH (95%, Strem). Mixing was performed with a Fritsch Pulverisette 23 miniMill using a stainless steel cup (10 mL) and four stainless steel balls (5 mm diameter) at 30 Hz for 15 min to form a slurry. The slurry was cast onto copper foil (0.127 mm, 99.9%, Alfa Aesar) and dried under vacuum at 150 °C for 2 h. Round electrodes (16 mm diameter) were cut from the resulting sheet using a die cutting press (MSK-T-07 Precision Disc Cutter, MTI Inc.). The areal mass of the electrode was 1.76 mg/cm$^2$.

Coin cells (CR2016, MTI Inc.) containing the BCG anode and Li metal (99.9%, MTI Inc.) electrodes separated by a polypropylene porous membrane (Celgard 3401) were assembled in an Ar-filled drybox (<0.1 ppm of $O_2$ and $H_2O$). The electrolyte used was 1 M LiPF$_6$ in an EC:DMC (1:1 v/v) mixture (battery grade, <15 ppm of $H_2O$ content, Sigma-Aldrich) with 10% FEC (>99%, Solvay) by volume. Electrochemical cycling was performed using an Arbin Instruments BT2000 battery test system. The cell was discharged (Li loading into BCG) at a constant current ($C/2$) from open circuit voltage to a cutoff potential of 10 mV Li/Li$^+$ and charged (Li unloaded from BCG) at the same current to 1.5 V vs Li/Li$^+$. The cells were rested for 15 min between discharge and charge cycles.

## ■ RESULTS AND DISCUSSION

BCG is produced by a two-step process, pyrolysis of biomass to produce bio-oil and biochar followed by the conversion of biochar to flake graphite. Following pyrolysis, pellets made from sawdust and −325 mesh Fe consisted of ~1−20 $\mu$m diameter Fe flakes, observed as high-contrast particles by SEM using a backscatter detector (Figure 1A), embedded in a
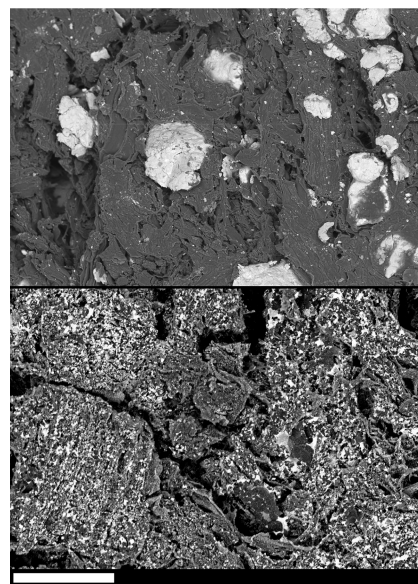


**Figure 1.** SEM images of pellet surface for biochar/Fe before (top) and after (bottom) laser irradiation (scalebar is 25 $\mu$m).

carbonaceous matrix (biochar). Exposing a pellet to the laser resulted in a bright orange glow, and the material appeared gray in color upon cooling. Exposure to the laser transformed the Fe flakes into more isotropically (spheroidal)-shaped, 1−5 $\mu$m particles that were more homogeneously distributed throughout the pellet (Figures 1B and 2), consistent with the Fe having been in a molten state. The surface temperature
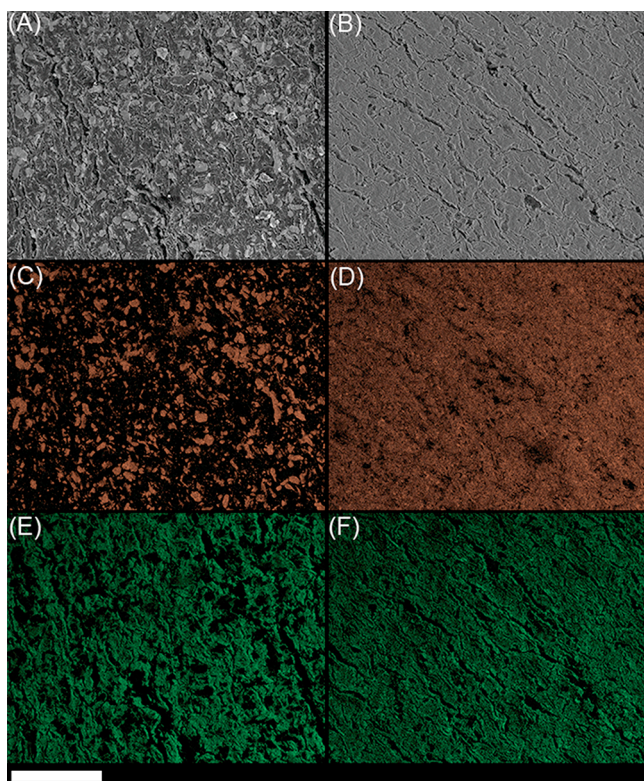
**Figure 2.** SEM image of a Fe/char pellet surface before (A) and after (B) laser irradiation. EDX elemental maps of Fe before and after laser irradiation appear in (C) and (D), respectively. C maps before and after laser irradiation appear in (E) and (F), respectively (scalebar is 500 $\mu$m).

at the center of the irradiated area of the pellet was found to be 1580 °C, high enough to melt Fe, Ni, or Co ($T_m$ = 1538, 1455, and 1495 °C, respectively), decreasing rapidly to 1290 °C approximately 1 mm from the irradiated spot. Analysis of the Fe content of material removed from the pellet prior to and after irradiation showed no change in composition, indicating that the Fe was not macroscopically transported during irradiation.

No evidence of graphite was found in the XRD patterns of the char prior to laser irradiation (Figure S1A). Cutting into the material after exposure to the laser resulted in a surface with a highly lustrous metallic sheen typical of graphite. XRD patterns of the material show a sharp peak consistent with the graphite (002) reflection (Figure S1B), with no evidence of metal carbide formation. XRD patterns of char that has been exposed to the laser in the absence of the metal do not show any evidence of graphite or the formation of any other crystalline phase.

SEM images of the purified BCG made with −325 mesh Fe reveals 10−30 $\mu$m diameter agglomerates of plate-like material consistent with agglomerates of flake graphite (Figure 3A). The plates are ∼5 $\mu$m wide, similar to the dimensions of the spheroidal metal particles observed in the material after exposure to the laser, and are ∼50 nm thick, with a significant fraction of the material consisting of smaller flakes. EDX spectra of the material show only carbon with no signal above the background for any other element. The BET surface area is 10.3(1) m$^2$/g and the pore volume 0.0508 cm$^3$/g, values that are significantly lower than we found, 17.6(1) m$^2$/g and 0.0546 cm$^3$/g, respectively, for a similar-sized flake commercial
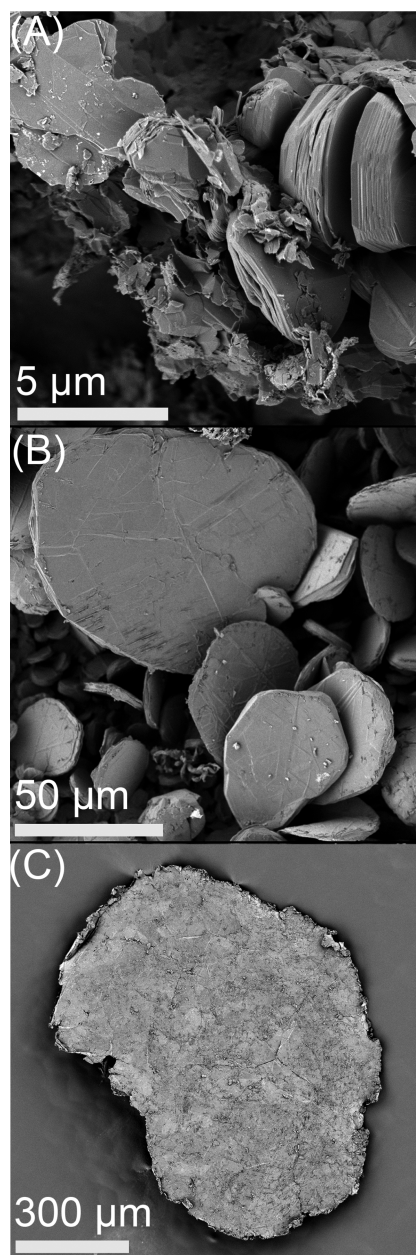


**Figure 3.** SEM images of purified BCG synthesized with (A) −325 mesh Fe, (B) 0.60 mm steel spheres, and (C) 1−2 mm Fe granules.

synthetic graphite (Imerys Timrex SFG6, d90 5.5−7.5 $\mu$m), indicating that the agglomerates are tightly packed. In fact, the agglomerates of BCG flakes look very similar to commercial Hitachi MAGE3 Li-ion battery "potato" graphite (Figure 4, S2), both in morphology and flake size. However, while BCG agglomerates are very densely packed (Figure S3), the surface area of BCG is more than twice that of the Hitachi MAGE3, consistent with it being somewhat less densely packed than the commercial potato graphite. Lowering the surface area is desirable for Li-ion battery graphite as it reduces the electrolyte/graphite interfacial area, decreasing initial irreversible losses.

The size of the flakes is dependent on the size of the metal particles used, with larger flakes formed from larger metal particles, ∼50−200 $\mu$m and ∼0.5−1 mm flakes with BET surface areas of 12.2(3) and 8.0(1) m$^2$/g and porsity of 0.0576 and 0.0493 cm$^3$/g from 0.60 mm spheres and 1−2 mm
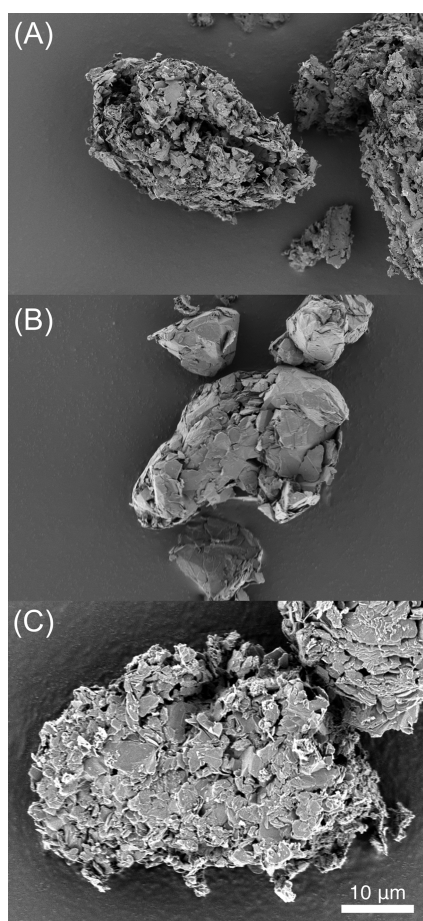
**Figure 4.** SEM images of purified BCG synthesized from (A) −325 mesh Fe and (C) Co, showing that they have very similar morphology to (B) Hitachi MAGE3 commercial potato graphite.

granules of Fe, respectively (Figure 3). The larger flakes of the agglomerates of the ∼50−200 $\mu$m BCG form radially from the metal core which becomes a cavity upon removal of the metal during purification. However, these larger flakes are not tightly packed in agglomerates as found for the smaller BCG, reflected both in SEM images and surface areas.

The XRD pattern of the BCG is consistent with graphite with no evidence of any other phase (Figure 5). Essentially identical XRD patterns are obtained regardless of which metal,
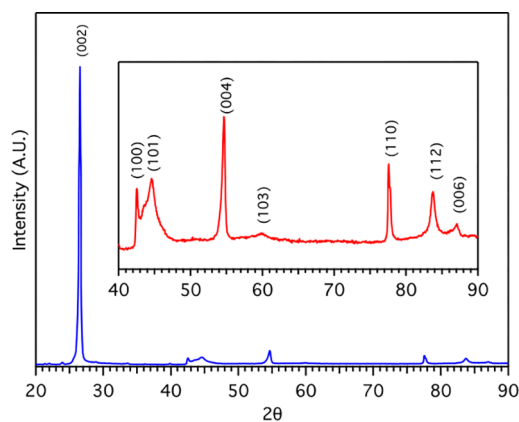


**Figure 5.** XRD pattern (blue) of ∼5 $\mu$m BCG. Inset scaled to show lower intensity reflections (red).

Fe, Co, or Ni, was used (Figure S4). Hexagonal (H-) and rhombohedral (R-) graphite consist of ABAB and ABC stacks of graphene layers, respectively, which are offset so that half of the carbon atoms occupy sites centered on the carbon hexagons of the adjacent layers. H-graphite is the thermodynamically favored structure; however, the enthalpic difference between the phases is small. Thus, while natural graphite is generally found to be (nearly) completely H-graphite,[19] synthetic graphite is generally a mixture of the two structures.[20] BCG made with −325 mesh Fe is 75% H-graphite and 25% R-graphite as determined by comparison of the integrated intensities of the respective (101) peaks.

Turbostratic carbon also consists of graphene layers and can have the same 2D crystalline order as graphite; however, random translation and rotation displacements of the layers result in imperfect matching of the adjacent graphene layers, increasing the interlayer spacing. The interlayer spacing of BCG made with −325 mesh Fe is 3.3546(5), determined by fitting its (002) peak (Figure S5), nearly identical to that of high-quality Sri Lanka natural lump graphite.[21,22] This shows a very low degree of turbostratic disorder or, equivalently, a very high degree of 3D graphitic order, which can be estimated to be >99.3% using eq 1.[23]

$$g = (3.44 - d_{002})/(3.44 - 3.354) \tag{1}$$

Analyzing the (002) peak width with the Scherrer equation allows one to find $L_c$, the average crystallite dimension along the graphene-stacking (c-) axis to be 32 nm, which is in reasonable agreement with the SEM observations. The average width in the graphene planes ($L_a$) of the crystallites can be similarly estimated from the (100) peak width to be 77 nm.[24]

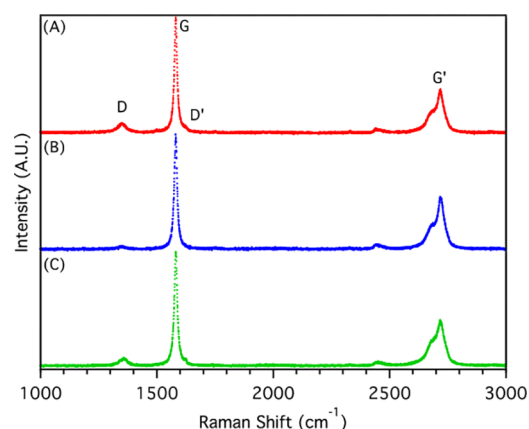Raman spectra of ∼5 $\mu$m and 0.5 to 1 mm BCG made with Fe, and SFG-6, are shown in Figure 6. The D-band (∼1350



**Figure 6.** Raman spectra of (A, red) SFG6, (B, blue) 0.5−1 mm BCG, and (C, green) ∼5 $\mu$m BCG.

cm$^{-1}$) and D′ (∼1620 cm$^{-1}$) arise from disorder (including graphene plane edges), while the G-band at ∼1580 cm$^{-1}$ is an allowed transition of the sp$^2$ carbon network of the graphene layers. The ratio of the intensities of the D and G bands, $I_D/I_G$, is a measure of the degree of order, allowing the calculation of the average distance between defects in the graphene planes ($L_a$).[25−27] The $I_D/I_G$ ratio of ∼5 $\mu$m BCG (0.15) is less than that of SFG6 (0.22),[20,28] with corresponding $L_a$ values of 128 and 87 nm, respectively, indicating that BCG has a higher degree of in-plane order. The very low $I_D/I_G$ ratio (0.04) of 0.5−1 mm BCG spectra and the absence of the D′ band, seen

as shoulders on the G bands of ~5 μm BCG and SFG-6, indicate a very high degree of order, with an $L_a$ value of 481 nm. The larger value is probably at least in part due to the much larger flake size, minimizing the contribution of crystallite edges to the spectra.

The degree of turbostratic structure can be found by deconvolution of the $G'$ (sometimes referred to as the 2D) band.[29] The presence of a $G'_{2D}$ band is indicative of turbostratic disorder. However, the $G'$ bands of each of these materials could be well fit with two peaks, $G'_{3DA}$ and $G'_{3DB}$, with no evidence of a $G'_{2D}$ band (Figure 7). This indicates that the materials all have very low turbostratic disorder, in agreement with XRD results.
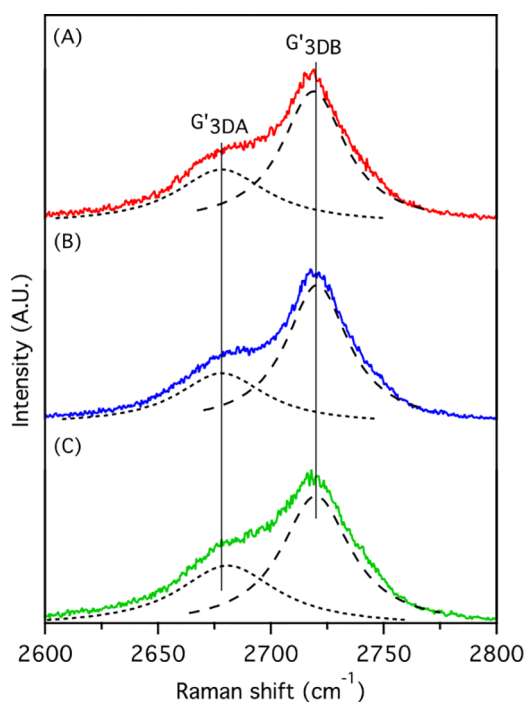


Figure 8. Differential of the charge and discharge capacity curves plotted as a function of cell potential for ~5 μm BCG from −325 mesh Fe (red, dashed lines) and Hitachi MAGE3 commercial potato graphite (blue, solid lines). The charge (lower) and discharge (upper) peak potentials of BCG are shifted to slightly lower potentials due to differences in the impedance of the test cells.



Figure 7. Raman spectra showing the $G'$ peaks (solid) and their deconvolution into $G'_{3DA}$ and $G'_{3DB}$ peaks (dashed) for (A, red) SFG6, (B, blue) 0.5−1 mm BCG, and (C, green) ~5 μm BCG.

BCG is nearly 100% carbon. The onset of mass loss of BCG made from −325 mesh Fe occurs in TGA thermograms at 770 °C, slightly higher than SFG6, with 100% mass loss by 1000 °C (Figure S6). Residual ash content is 0.02(2)%, somewhat lower than SFG6 (0.07%). Elemental analysis by GDMS indicates 99.95% graphite purity with a total of 526 ppm of impurity elements above the detection limits (Table S1). The purity is comparable to high (battery)-grade commercial synthetic graphite[30] but with notably low levels of S, Si, Zr, and W content and high Na, Cl, and Fe content. In fact, 79% of the impurities found in BCG are Na, Cl, and Fe, elements that could likely be further reduced by additional washing. Low impurity levels are particularly important for high-value applications, including carbon raisers, EDM electrodes, carbon brushes, and batteries. The very low level of S in BCG is particularly significant as its presence is highly undesirable due to its corrosive effects.

The performance of BCG as an anode active material is essentially the same as commercial Li-ion grade graphite, with nearly identical charge/discharge curves (Figure 8) and
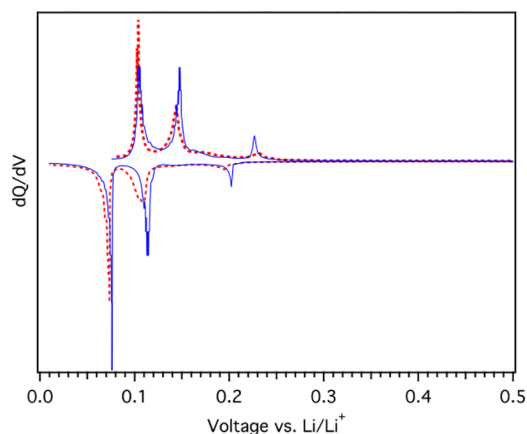
excellent capacity and cycle life regardless of whether it was made using Fe (Figure 9), Co (Figure S7), or Ni (Figure S8).



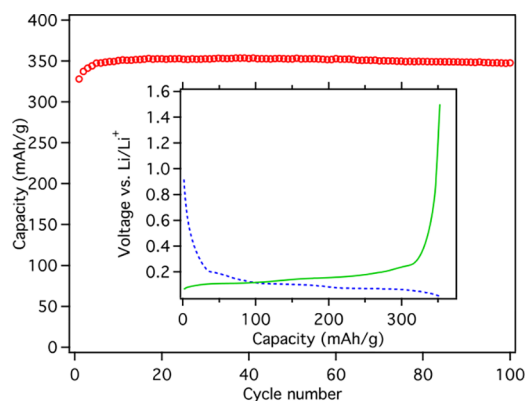Figure 9. Gravimetric capacity of a ~5 μm BCG (made from −325 mesh Fe) anode demonstrating excellent Li-ion capacity (353 mA/g, red circles), comparable to that of commercial Li-ion battery grade graphite with only a 1% capacity loss over 100 charge/discharge cycles at a C/2 rate. Inset is its charge (blue dashed line)/discharge (green line) profile, which is, again, nearly identical to commercial graphite.

The first cycle Coulombic efficiency (CE) of BCG anodes made with sawdust and −325 mesh Fe is ~84%, matching that of commercial Li-ion with a similar surface area, but lower than the significantly lower surface area Hitachi MAGE3 (~91%). This suggests that the performance of BCG Li-ion anodes may be improved by further densification of its agglomerates, lowering the surface area to increase the initial CE.

The total product yield after purification was 84 wt % of the pre-laser pyrolysis biochar mass. The charred biomass was found to consist of 87.74% C, 2.82% H, 0.29% N, and 4.68% O; thus, 95.7% of the C in the biochar was converted to graphite. This very high yield means that while simple dissolution of C into liquid Fe and its precipitation upon cooling could initiate growth, analogous to the formation of Kish graphite during iron smelting,[31,32] it probably cannot account for the bulk of the graphite formation. The mass of graphite synthesized is 32.4% of the combined graphite and Fe

mass in the final reaction mixture, while the solubility of C in liquid Fe is only ~5.3% (w/w) at the highest temperature observed or 6.7% as the metastable phase $Fe_3C$.[33] Thus, if the Fe was saturated with C or even if it was all converted to $Fe_3C$, the precipitation of the dissolved C, or decomposition of the $Fe_3C$, upon cooling would account for less than 20% of C converted to graphite. Note that C is soluble to a similar extent in Ni and Co.

The extremely high fraction of the biochar carbon that is converted to graphite is in contrast to that found for the analogous laser pyrolysis production of hollow carbon nanospheres (HCNS) from the char of biomass/metal salt mixtures.[34] Both processes result in the growth of graphene layers from metal particles, the metal salts being transformed to metal nanoparticles during charring or laser pyrolysis when making HCNS. However, HCNS are not graphite; rather, they are nested graphene layers, necessarily turbostratic due to their curvature and as demonstrated by their interlayer spacing (3.41 Å), that grow tangentially to the surface of and surround the metal core. Furthermore, the carbon content of the HCNS does not exceed that which is soluble in the molten metal, consistent with shell formation by precipitation from the metal cores upon cooling.

The initial stages of the formation of BCG seem likely to closely resemble the formation of HCNS, that is, the precipitation of graphene shells surrounding the metal, with the first shell solidifying on the metal surface and subsequent shells growing from the inside. However, the metal cores of HCNS have radii on the order of 15−20 nm, giving them a surface to volume ratio that is ~2 orders larger than the smallest (−325 mesh) metal used here to produce graphite. Thus, while the tens of graphene layers that precipitate to form HCNS clearly do so largely without creating enough internal pressure to rupture the shells, the large carbon content of the micrometer-scale metal used to produce flake graphite creates fractures in the graphene layers as additional layers are formed on the relatively small surface area. This becomes more dramatic when graphite is made with larger (~50−200 $\mu$m) Fe metal, as the larger flakes of graphite emanate radially rather than tangentially to the metal surface. The fracturing of the shells allows the graphene layers to relax into the thermodynamically favored co-planar, rather than curved, orientation and form a 3D graphitic structure by slipping into alignment.

The very high carbon utilization observed seems likely to be due to the formation of graphite emanating from the metal particles, rather than graphene shells surrounding them. Non-graphitizable carbons such as biochar form strong cross-linked networked micro-domains that prevent graphitization even when heated to 3000 °C.[35] Laser pyrolysis of biochar results in extremely rapid heating ($\sim10^3-10^4$ °C s$^{-1}$), transforming the char into reactive intermediates, including molecular poly-aromatic species.[36−37] Thus, it may disrupt the cross-linked micro-domains, transforming the biochar to graphitizable species. However, this reservoir of graphitizable species may not be well coupled to the graphene shells that grow tangentially to the metal surface and thus contribute little to growth. In contrast, the graphite seeds that grow from the metal are able to add carbon from the biochar, by translation of the molten metal ahead of precipitating graphite, extension of the graphite into the biochar, or through preferential growth at prismatic faces, providing the bulk of the carbonaceous species for growth.

Results that are similar to those described above can be achieve with any number of biomass starting materials. The synthesis of BCG has been confirmed from two different sawdust sources and corncob, as well as individual biomass components lignin and cellulose (Figure S9). Other carbonaceous materials can be used as well, including lignite (Figure S10), a non-graphitizable coal that is a particularly inexpensive alternative.

## CONCLUSIONS

In summary, biochar can be rapidly converted to Li-ion grade, highly crystalline flake graphite by laser pyrolysis with a very high yield (95.7%). The dimensions of metal particles embedded in the biochar determine the flake size of the graphite product. Using smaller metal particles results in agglomerates of 1−5 $\mu$m graphite flakes that are very similar to commercial Li-ion battery "potato"-shaped graphite. It seems likely that the process should be widely applicable to available carbonaceous materials, including biomass from agricultural waste, industrial/municipal waste or energy crops, or alternative carbonaceous materials, such as coal, peat, or petroleum products.

In conclusion, the conversion of biochar to graphite described above is an enormous step forward in the sustainable production of Li-ion grade graphite. It avoids the voluminous greenhouse emissions of commercial synthetic graphite production, instead providing a carbon negative route. It eliminates the devastating environmental impacts to soil, water, and air caused by mining graphite, including the large-scale use of HF, instead using potentially much smaller quantities of HCl, an acid that satisfies the United States Environmental Protection Agency's "Safer Choice Criteria" as a "best-in-class chemical". Furthermore, one could consider the proposed route to be a modification of a current commercial method of producing ferrous chloride, the dissolution of Fe with HCl, with the added benefit of high-grade carbon negative graphite production with little or no additional environmental impact. Finally, the production of graphite from biochar could provide a value-added product to greatly enhance the economic viability of carbon neutral bio-oil production.

## ASSOCIATED CONTENT

**Ⓢ Supporting Information**

The Supporting Information is available free of charge on the ACS Publications website at DOI: 10.1021/acssuschemeng.8b02799.

> Additional figures, elemental analysis results, and economic analysis (PDF)

## AUTHOR INFORMATION

**Corresponding Author**
*E-mail: wagnerm@gwu.edu.

**ORCID** ⓘ
Michael J. Wagner: 0000-0001-9559-7804

**Present Address**
800 22nd Street NW, Suite 4000, Department of Chemistry, George Washington University, Washington, DC 20052, USA.

**Notes**
The authors declare no competing financial interest.

## ■ ACKNOWLEDGMENTS

## ■ REFERENCES

(1) Woolf, D.; Lehmann, J.; Lee, D. R. Optimal Bioenegy Power Generation for Climate Change Mitigation With or Without Carbon Sequestration. *Nat. Commun.* **2016**, *7*, 13160.

(2) Lee, J. W.; Hawkins, B.; Day, D. M.; Reicosky, D. C. Sustainability: the capacity of smokeless biomass pyrolysis for energy production, global carbon capture and sequestration. *Energy Environ. Sci.* **2010**, *3* (11), 1695−1705.

(3) Bhutto, A. W.; Qureshi, K.; Abro, R.; Harijan, K.; Zhao, Z.; Bazmi, A. A.; Abbas, T.; Yu, G. Progress in the production of biomass-to-liquid biofuels to decarbonize the transport sector - prospects and challenges. *RSC Adv.* **2016**, *6* (38), 32140−32170.

(4) Wang, G.-H.; Cao, Z.; Gu, D.; Pfander, N.; Swertz, A. C.; Spliethoff, B.; Bongard, H. J.; Weidenthaler, C.; Schmidt, W.; Rinaldi, R.; Schuth, F. Nitrogen-Doped Ordered Mesoporous Carbon Supported Bimetallic PtCo Nanoparticles for Upgrading of Bio-phenolics. *Angew. Chem., Int. Ed.* **2016**, *55*, 8850−8855.

(5) Lee, H.; Kim, H.; Yu, M. J.; Ko, C. H.; Jeon, J.-K.; Jae, J.; Park, S. H.; Jung, S.-C.; Park, Y.-K. Catalytic Hydrodeoxygenation of Bio-oil Model Compounds over Pt/HY Catalyst. *Sci. Rep.* **2016**, *6* (28765), 1−7.

(6) Zhang, X.-S.; Yang, G.-X.; Jiang, H.; Liu, W.-J.; Ding, H.-S. Mass production of chemicals from biomass-derived oil by directly atmospheric distillation coupled with co-pyrolysis. *Sci. Rep.* **2013**, *3* (1120), 1−7.

(7) Gumidyala, A.; Wang, B.; Crossley, S. Direct carbon-carbon coupling of furanics with acetic acid over Brønsted zeolites. *Science Advances* **2016**, *2* (9), 1−7.

(8) Vispute, T. P.; Zhang, H.; Sanna, A.; Xiao, R.; Huber, G. W. Renewable Chemical Commodity Feedstocks from Integrated Catalytic Processing of Pyrolysis Oils. *Science* **2010**, *330* (6008), 1222.

(9) Woolf, D.; Amonette, J. E.; Street-Perrott, F. A.; Lehmann, J.; Joseph, S. Sustainable biochar to mitigate global climate change. *Nat. Commun.* **2010**, *1*, 56.

(10) Alonso, D. M.; Hakim, S. H.; Zhou, S.; Won, W.; Hosseinaei, O.; Tao, J.; Garcia-Negron, V.; Motagamwala, A. H.; Mellmer, M. A.; Huang, K.; Houtman, C. J.; Labbé, N.; Harper, D. P.; Maravelias, C. T.; Runge, T.; Dumesic, J. A. Increasing the revenue from lignocellulosic biomass: Maximizing feedstock utilization. *Science Advances* **2017**, *3* (5), 1−7.

(11) Emerald Insight.. Global Graphite Market Will Reach US $17.56 billion in Terms of Value and 4.48 Million Tons in Terms of Volume, in 2020. *Anti-Corros. Methods Mater.* **2015**, *62*, 1.

(12) Chung, D.; Elgqvist, E.; Santhanagopalan, S. *Automotive Lithium-ion Battery Supply Chain and US Competitiveness Considerations*; Clean Energy Manufacturing Analysis Center: 2015.

(13) Menéndez-Díaz, J. A.; Martín-Gullón, I. Types of carbon adsorbents and their production. In *Activated Carbon Surfaces in Environmental Remediation*; Bandosz, T. J., Ed.; Elsevier: 2006; Vol. 7, pp 1−47.

(14) Dunn, J. B.; James, C.; Gaines, L.; Gallagher, K.; Dai, Q.; Kelly, J. C. *Material and Energy Flows in the Production of Cathode and Anode Materials for Lithium Ion Batteries*; Argonne National Lab: 2015.

(15) Whoriskey, P. *In Your Phone, In Their Air*; The Washington Post: 2016.

(16) Olson, D. W.; Virta, R. L.; Mahdavi, M.; Sangine, E. S.; Fortier, S. M. Natural graphite demand and supply - Implications for electric vehicle battery requirements. *Spec. Pap. - Geol. Soc. Am.* **2016**, *520*, 67−77.

(17) Graphite Demand From Lithium Ion Batteries to More than Treble in 4 Years. *Benchmark Mineral Intelligence*; Benchmark Mineral Intelligence: 2016; http://www.benchmarkminerals.com/graphite-demand-from-lithium-ion-batteries-to-more-than-treble-in-4-years/.

(18) Moores, S. Battery grade graphite shortage on horizon as demand rockets. *Benchmark Magazine*; Benchmark Mineral Intelligence: 2016; pp 14−16.

(19) Laves, F.; Baskin, Y. *On the Formation of the Rhombohedral Graphite Modification* **1956**, *107*, 337−356.

(20) Buqa, H.; Würsig, A.; Goers, D.; Hardwick, L. J.; Holzapfel, M.; Novak, P.; Krumeich, F.; Spahr, M. *J. Power Sources* **2005**, *146*, 134−141.

(21) Kalyoncu, R. S.; Taylor, H. A.; Degee, P. Natural Graphite. *Kirk-Othmer Encyclopedia of Chemical Technology* **2004**, *12*, 1.

(22) Zhao, G.; Qian, S. a.; Tao, K. Study on the structural characteristics of graphitized carbon microcrystal prepared from PI film using X-ray diffraction technique. *Sci. China, Ser. E: Technol. Sci.* **1998**, *41* (1), 1−5.

(23) Flandrois, S.; Simon, B. *Carbon* **1999**, *37*, 165−180.

(24) Warren, B. E. X-Ray Diffraction Study of Carbon Black. *J. Chem. Phys.* **1934**, *2* (9), 551−555.

(25) Cançado, L. G.; Takai, K.; Enoki, T.; Endo, M.; Kim, Y. A.; Mizusaki, H.; Jorio, A.; Coelho, L. N.; Magalhães-Paniago, R.; Pimenta, M. A. General equation for the determination of the crystallite size La of nanographite by Raman spectroscopy. *Appl. Phys. Lett.* **2006**, *88* (16), 163106.

(26) Pimenta, M. A.; Dresselhaus, G.; Dresselhaus, M. S.; Cancado, L. G.; Jorio, A.; Saito, R. Studying disorder in graphite-based systems by Raman spectroscopy. *Phys. Chem. Chem. Phys.* **2007**, *9* (11), 1276−1290.

(27) Ferrari, A. *Solid State Commun.* **2007**, *143*, 47−57.

(28) Sole, C. E.; Drewett, N.; Liu, F.; Abdelkader, A.; Kinloch, I.; Hardwick, L. J. The role of re-aggregation on the performance of electrochemically exfoliated many-layer graphene for Li-ion batteries. *Journal of Electroanalytical Chemistry* **2015**, *753*, 35.

(29) Cançado, L.; Takai, K.; Enoki, T.; Endo, M.; Kim, Y.; Mizusaki, H.; Speziali, N.; Jorio, A.; Pimenta, M. Measuring the degree of stacking order in graphite by Raman spectroscopy. *Carbon* **2008**, *46*, 272.

(30) Trammell, M. P.; Pappano, P. J. *Analysis of Natural Graphite, Synthetic Graphite, and Thermosetting Resin Candidates for Use in Fuel Compact Matrix*, ORNL/TM-2011/315; Oak Ridge National Laboratory: Oak Ridge, TN, 2011.

(31) Oberlin, a.; Rouchy, J. P. Transformation des carbones non graphitables par traitement thermique en presence de fer. *Carbon* **1971**, *9*, 39−42.

(32) Liu, S.; Loper, C. R., Jr. The formation of kish graphite. *Carbon* **1991**, *29*, 547−555.

(33) Okamoto, O. The C-Fe (Carbon-Iron) System. *J. Phase Equilib.* **1992**, *13*, 543−565.

(34) Herring, A. M.; McKinnon, J. T.; McCloskey, B. D.; Filley, J.; Gneshin, K. W.; Pavelka, R. A.; Kleebe, H.-J.; Aldrich, D. J. A Novel Method for the Templated Synthesis of Homogeneous Samples of Hollow Carbon Nanospheres from Cellulose Chars. *J. Am. Chem. Soc.* **2003**, *125* (33), 9916−9917.

(35) Franklin, R. E. Crystallite growth in graphitizing and non-graphitizing carbons. *Proc. R. Soc. London, Ser. A* **1951**, *209* (1097), 196.

(36) Herring, A. M.; McKinnon, J. T.; Petrick, D. E.; Gneshin, K. W.; Filley, J.; McCloskey, B. D. Detection of reactive intermediates

during laser pyrolysis of cellulose char by molecular beam mass spectroscopy, implications for the formation of polycyclic aromatic hydrocarbons. *J. Anal. Appl. Pyrolysis* **2003**, *66* (1−2), 165−182.

(37) Herring, A.; Thomas McKinnon, J.; Gneshin, K. W.; Pavelka, R.; Petrick, D. E.; McCloskey, B.; Filley, J. Detection of reactive intermediates from and characterization of biomass char by laser pyrolysis molecular beam mass spectroscopy. *Fuel* **2004**, *83*, 1483−1494.